Applied Acoustics 169 (2020) 107457

Contents lists available at ScienceDirect

Applied Acoustics

journal homepage: www.elsevier.com/locate/apacoust

Benchmarking the vibration velocity-based measurement methods to determine the radiated sound power from floor elements under impact excitation

Simone Conta [a,*], Andrea Santoni [b], Anders Homb [a,c]

[a] NTNU, Department of Civil and Environmental Engineering, 7491 Trondheim, Norway
[b] Università degli Studi di Ferrara, Dipartimento di Ingegneria, 44122 Ferrara, Italy
[c] SINTEF Community, 7465 Trondheim, Norway

ARTICLE INFO

Article history:
Received 26 March 2020
Received in revised form 26 May 2020
Accepted 26 May 2020
Available online 30 June 2020

Keywords:
Radiated sound power
Building acoustic
Rayleigh integral method
Integral transform method
Impact sound insulation
Discrete calculation method

ABSTRACT

The Rayleigh Integral Method, the Integral Transform Method and the Discrete Calculation Method are all vibration velocity-based measurement methods to determine the radiated sound power from planar objects. Even though all these three methods are based on a well-established theoretical background, which has been known for long time, they are only now gaining popularity in the building acoustics field and the building acoustics community is still rather new to them. They offer advantages compared to the standard methods specially in the low frequency range or on special applications with articulated boundary conditions. In this paper, we want to summarize the three methods in one place to highlight their different theoretical foundations. We present a numerical benchmark of these three methods, based on a simple panel with varying boundary conditions, highlighting similarities and differences between them. In a second step, we compare the radiated sound power levels obtained by the three methods with results obtained by a standard measurement procedure according to the ISO 10140-3, under excitation by an ISO tapping machine. Finally, we present the application of the methods to determine the *in-situ* impact noise level of a floor structure: a complex system with challenging boundary conditions. The results show a good agreement between all the tested methods, as long as the respective requirements are satisfied. The results also demonstrate how the vibration velocity-based measurement methods can have a broader application compared to the standard laboratory method and deliver additional information on complex test objects.

1. Introduction

Building acoustic measurements are generally carried out according to appropriate standards. When looking at the impact sound insulation the relevant standards for laboratory measurements is the ISO 10140-3 [1]. The well-known measurement method described therein is based on impact excitation by means of an ISO tapping machine and measurement of the sound pressure level in the receiving room. The accuracy of the results in the low frequencies is limited because the sound field is not diffuse. This point is rather critical considering that frequencies below 50 Hz are of great importance when considering impact sound insulation and annoyance in lightweight buildings [2]. Because of this and the fact that scanning laser vibrometers and multichannel measurement systems are nowadays available in many laboratories, hybrid experimental methods based on vibration velocity measurements are becoming increasingly popular. They are indeed complementary to the standard methods since they offer increased accuracy at low frequencies and set less stringent requirements to the measurement environment. This last point is an advantage also compared to intensity measurements, that require a highly damped receiving room.

The sound power radiated by a vibrating element can be evaluated, from the experimental measurement of the vibration velocity over its surface, by means of at least three different approaches: the Rayleigh Integral Method (RIM) [3], the Discrete Calculation Method (DCM) [4] and the Integral Transform Method (ITM) [5]. All the three methods have been proven to be accurate and reliable to determine the sound power radiated from planar objects, at least if certain requirements are fulfilled [6–13]. The study presented in this paper was driven by two main motivations: i) in the building acoustics community these methods are still rather

* Corresponding author at: Institutt for bygg- og miljøteknikk, NTNU, Gløshaugen: Høgskoleringen 7a, 7491 Trondheim, Norway.
E-mail address: Simone.Conta@ntnu.no (S. Conta).

https://doi.org/10.1016/j.apacoust.2020.107457
0003-682X/

new, and the differences and respective peculiarities are not well known. A thorough and systematic comparative analysis of this methods is still missing and might help to spread the knowledge about them. ii) These methods were previously employed to evaluate the acoustic performance of building elements, either acoustically or mechanically excited, also comparing the obtained results with results determined by standard sound pressure measurements. However, to the authors' best knowledge, the application of these methods to determine the impact sound level generated by an ISO tapping machine has never been thoroughly investigated.

This paper has three main objectives: i) to provide a systematic and critical comparison of the three measurement methods RIM, DCM and ITM, ii) to evaluate the accuracy and the reliability of these methods to measure the impact sound insulation of complex building elements, with articulated boundary conditions, excited by the ISO tapping machine. The validation was performed by comparing the results of the methods under investigation with laboratory measurements performed according to the standard ISO 10140-3; iii) to investigate to what extent the boundary conditions of the considered structure might represent a limitation for the investigated method.

Firstly, we prepared a finite element (FE) model of a thin aluminium plate and calculated the vibration velocity distribution over the plate surface. From this data, we calculated the radiation efficiency of the plate with the three different methods. These results were used to benchmark the three methods, in order to identify limitations, differences and similarities. Moreover, the effect of varying boundary conditions was also investigated to identify possible shortcomings of each method, especially regarding the ITM. Secondly, we measured the impact sound level of a floor element in an acoustic laboratory with the traditional measurements according to the ISO 10140-3 standard and we recorded in parallel the vibration velocity. Assuming perfect diffuse field conditions, we converted the impact sound level in radiated sound power and compared the obtained values with the results determined by the hybrid methods. The analysis allowed us to asses whether RIM, ITM and DCM are reliable alternative to the standard methods for determining the impact noise level under excitation with an ISO tapping machine. Finally, we present an application example. We considered here a timber hollow-box floor installed on the mock-up of a structural system with moment resisting connections. We compared the radiated sound power under impact excitation measured *in-situ* by DCM and ITM with that measured in the lab following ISO 10140-3. We compare the results and discuss the differences obtained.

In the next section, the three hybrid investigated approaches are introduced. Section 3 describes in detail the methodology adopted and the experimental setups. Section 4 presents the results and finally Section 5 includes the conclusions.

2. Measurement methods

2.1. Measurements according to ISO 10140-3

The standard ISO 10140-3 provides the procedure and the requirements to perform laboratory measurements of impact sound level. This standard is well-known, and we shall recall here just a few elements for the sake of clarity and ease of reference.

The laboratory setup comprises two rooms, placed one above the other, separated by the floor under test. The excitation source is placed at several positions on top of the floor and the sound pressure level is measured in the lower room. The normalized impact sound pressure levels L_n are calculated from the energy averaged sound pressure levels in the receiving room and the measured reverberation times. In this study, an ISO tapping machine, described in the ISO 10140–5, was used as impact source. According to the standard, the normalised impact sound pressure level L_n is determined by normalising the measured sound pressure level L_i with respect to the equivalent absorption area A in the receiving room:

$$L_n = L_i + 10\log\frac{A}{A_0}\,(\mathrm{dB}) \tag{1}$$

where A_0 = 10 m^2. The normalised impact sound pressure level determined according to the standard procedure can be converted to a sound power level using the following equation, based on a diffuse field assumption [13,14]:

$$L_W = L_n + 4\ (\mathrm{dB}) \tag{2}$$

The assumption is strictly valid above the Schroeder Frequency, in our case above ~200 Hz.

The limitations of this approach are related to the sound field in the receiving room. At low frequencies the sound field in the receiving room is not diffuse leading to a large standard deviation in the measurements. It has been also shown that due to strong modal coupling between floor element and receiving room, the accuracy in the determination of the floor properties might be limited [7]. Moreover, further limitations are of more practical character, e.g. the size of the laboratory opening and the mounting of the floor element, which is generally limited to boundary conditions close to simply supported.

2.2. Rayleigh Integral Method

The Rayleigh Integral Method (RIM) is one of the classical approaches used to describe the sound radiation from a planar object, describing it in terms of a sum of point sources [3,14–16]. The sound pressure p at a point R at a time t can be calculated from the complex normal surface velocity $\widehat{v}_n(r_s)$ on the vibrating surface S at the position r_s with following relation:

$$p(R,t) = j\frac{\rho_0 c_0 k_0}{2\pi}\oint_S \frac{\widehat{v}_n(r_s)\cdot e^{j(\omega t - k_0 r)}}{r}dS \tag{3}$$

or in its discretized form:

$$p(R,t) = j\frac{\rho_0 c_0 k_0}{2\pi}\sum_i \frac{\widehat{v}_n(r_{s,i})\cdot e^{j(\omega t - k_0 r_i)}\cdot S_i}{r_i} \tag{4}$$

where ρ_0 is the density of air, c_0 is the speed of sound in air, ω is the angular frequency, k_0 is the acoustic wavenumber, $r_i = |R - r_{s,i}|$ indicates the distance between the plate's vibrating element i with area S_i and the position R, j is the imaginary unit.

We can use Eq. (4) to calculate the sound pressure distribution over an imaginary hemisphere centred around the vibrating surface. Then, we can calculate the radiated sound power W by integrating the root mean square sound pressure p^2 over the surface of the hemisphere Ω [6,14]:

$$W = \oint_\Omega \frac{\tilde{p^2}}{\rho_0 c_0}\cdot d\Omega \tag{5}$$

or in its discretized form:

$$W = \sum_i \frac{\tilde{p_i^2}\cdot\Omega_i}{\rho_0 c_0} \tag{6}$$

The above equations are valid only under the assumption of a locally plane wave field and under free-field conditions. The requirement of a locally plane wave imposes that the radius of hemisphere, over which the sound pressure is computed, is sufficiently large. Also, the discretisation of points over the hemisphere

surface must be fine enough to capture the details of the sound radiation pattern. Both aspects can be easily checked by a trial and error procedure and verification that the results do not depend on the settings of the calculation. Alternatively, one could calculate the sound intensity directly at the interface between the fluid and the vibrating element ($z = 0$, with z the cartesian axis perpendicular to the panel surface) and integrate over its surface [7]. The two approaches are equivalent. The second approach requires a slightly more advanced mathematical formulation but avoids the calculation over the large amount of points on the sphere. In the current paper, we used the first approach.

The spatial discretisation of the radiating plate must consider the Nyquist-Shannon sampling theorem and the velocity of the bending waves propagating through the panel. The requirements of the theorem must be fulfilled over the whole frequency range of interest. If Δx, Δy are the size of the i^{th} element of the plate and $\lambda_{b,x}$, $\lambda_{b,y}$ are the wavelength of the bending waves in the panel along the x and y direction respectively:

$$\Delta x < \frac{\lambda_{b,x}}{2}, \Delta y < \frac{\lambda_{b,y}}{2}. \tag{7}$$

2.3. Integral Transform Method

The Integral Transform Method is an alternative classical approach to the determination of the radiated sound power from planar objects and its theoretical approach was already described by Heckl in [5]. Williams and Maynard described the same method and discussed the details of its implementation in [17].

The sound power W radiated by a surface S can be calculated from the sound pressure $p(x,y,z = 0) = p_s(x,y)$ on the surface of the vibrating structure and from the complex normal surface velocity $\widehat{v}_n(x,y)$ on the vibrating surface S at the position (x,y) with the well know relation [18]:

$$W = \frac{1}{2} Re\left\{ \iint_{-\infty}^{+\infty} p_s(x,y)\, \widehat{v}_n(x,y)^* dxdy \right\} \tag{8}$$

which corresponds to integrating the sound intensity over the radiating surface. By using the Rayleigh-Parseval theorem and the expression for the sound pressure from a plane radiator described as a sum of plane waves [5], the above equation can be rewritten as [18]:

$$W(f) = \frac{1}{2} \frac{\rho_0 c_0}{4\pi^2} \mathrm{Re}\left\{ \iint_{-\infty}^{+\infty} \frac{k_0(f)}{\sqrt{k_0^2(f) - k_x^2 - k_y^2}} \left|\widehat{v}(k_x, k_y, f)\right|^2 dk_x dk_y \right\} \tag{9}$$

where the dependency on the frequency f is explicited, $\widehat{v}(k_x, k_y, f)$ is the complex vibration velocity of the plate surface expressed in the wavenumber domain, i.e. the 2-D Fourier transform of plate vibration velocity, k_0 is the wavenumber in air and k_x, k_y are the wavenumber components of the structural waves in the plate, respectively along the x and y direction.

For the purpose of this paper, we implemented the procedure following the approach presented in [11], which we refer the reader to for the implementation details. For ease of reference, we indicate here the discretized form of Eq. (9) for the radiated sound power W:

$$W(\gamma) = \frac{1}{2} \frac{\rho_0 c_0}{4\pi^2} \mathrm{Re}\left\{ \sum_{\alpha=1}^{M_\alpha} \sum_{\beta=1}^{M_\beta} \frac{k_0(\gamma)}{\sqrt{k_0(\gamma)^2 - (\alpha\Delta k_x)^2 - (\beta\Delta k_y)^2}} \left|\widehat{v}(\alpha,\beta,\gamma)\right|^2 \Delta x^2 \Delta y^2 \right\} \Delta k_x \Delta k_y \tag{10}$$

where γ indicates the discrete frequency step, α, β are the coordinates in the wavenumber domain, $M_\alpha = z_p \frac{l}{\Delta x}$ and $M_\beta = z_p \frac{w}{\Delta y}$ represent the number of samples in the wavenumber domain with $l \times w$ the dimensions of the plate, with z_p the zero padding factor required in the 2-D Fourier transform; $\Delta x, \Delta y$ is the grid size of the vibration velocity measurements (i.e. the dimensions of the plate divided by the number of grid points in the respective directions) and $\Delta k_x = \frac{2\pi}{z_p l}, \Delta k_y = \frac{2\pi}{z_p w}$ is the resolution in the wavenumber domain. In the practical usage of this relationship, the vibration velocity in the wavenumber domain will be calculate with a 2-D Fourier transform of the measured vibration velocity field at each frequency step γ. Many of the practical challenges are shared here with acoustic holography. An example is the use of the zero padding to reduce wraparound errors and obtain an adequate aperture size [17,19,20]. It is interesting to note here that Williams and Maynard already showed that the use of zero padding does not create any limitation with respect to the plate boundary condition, even in the extreme case of all the edges in a free condition (F-F-F-F BCs).

The measurement of the vibration velocity on the plate underlies the Nyquist-Shannon sampling theorem requirements for the Integral Transform Method in the same manner as it is for the RIM. Further aspects must be considered when assessing the limit of validity of the ITM method: they include the bias error, the bending wave velocity in the measurement object and the decay of the side lobes.

The bias error is due to the numerical singularity that arises whenever the wavelength or a multiple of it matches the size of the aperture. This problem can be tackled either by refining the numerical procedure to contain the singularity [11,17] or by further increasing the zero padding factor. Both approaches deliver comparable results.

To discuss the further requirements of ITM, it is helpful to introduce a few diagrams. Fig. 1 shows typical wavenumber plots obtained during the analysis procedure with the ITM. In the wavenumber versus frequency diagram (a) we recognise the dispersion curve of the structural waves k_b, highlighted by the dashed line. For reference, the wavenumber of the soundwaves in air k_0 is plotted as a solid line. A closer look at selected frequencies reveals the specific features of the spectrum (diagrams b and c of Fig. 1): the main peaks represent the vibrational modes of the plate. The side lobes are given by the finite size of the panel and the boundary conditions, which also have a strong influence on their decay. From Eq. (10), it follows that only the area within the radiation circle with radius k_0 contributes to the sound radiation. In Fig. 1a, the same area is that between the two solid lines. Therefore, the side lobes are a major contribution to the radiated sound power, especially for frequencies below the critical frequency f_c. Considerations about aliasing must include the side lobes. As a good rule of thumb, to avoid aliasing the side lobes must decay considerably before reaching k_{max}.

Fig. 2 shows idealized curves for the following three cases and the respective upper limits of the method. Case a): the frequency f_{max} at which the structural wave dispersion curve reaches the limit $k_{x,max} = \frac{\pi}{\Delta x}$ (determined by the Nyquist-Shannon theorem requirements on the grid spacing) is well below the critical frequency f_c of the ITM. In this case f_{max} is the upper limit of validity of the ITM. The limit might be slightly lower depending on the measurement setup and the boundary conditions. In the case of orthotropic plates, or a different grid size along the x and the y direction, the lowest frequency limit must be considered. Case b): the critical frequency f_c is close to the frequency f_0 at which the wavenumber of sound waves in air reaches the limiting wavenumber: $k_0 = k_{max}$. In this case f_0 is the upper limit at which the ITM method delivers reliable results. This limit is best visualised by looking at Fig. 1c and considering that i) the sum of Eq. (10) is performed over the whole wavenumber domain showed by the diagram and ii) the surface within the radiation circle k_0 contributes to sound radia-

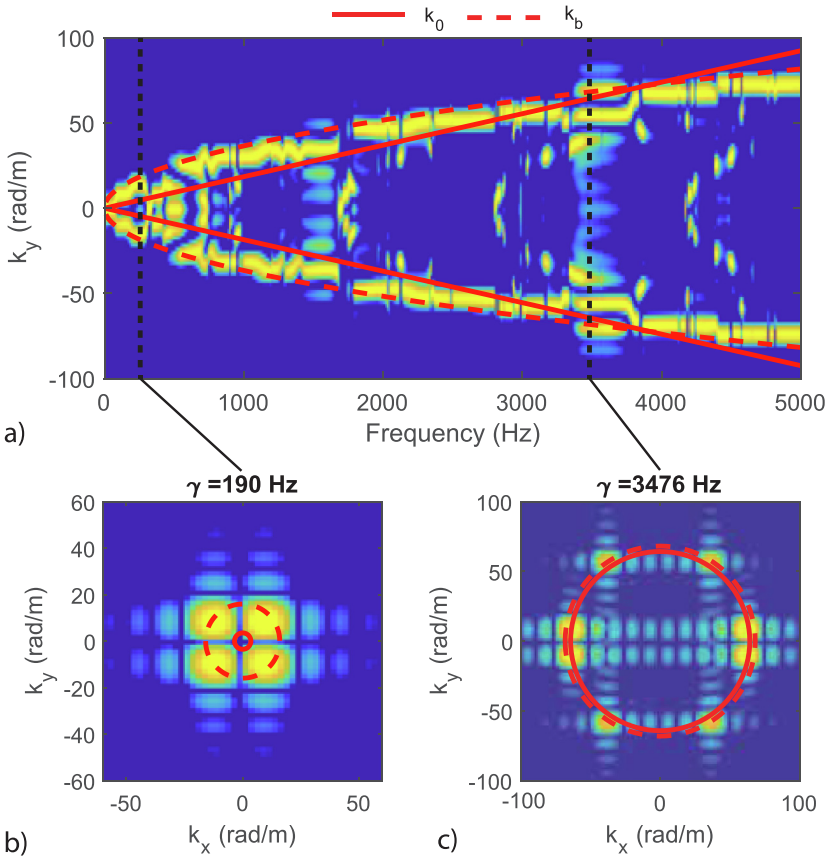

Fig. 1. Typical wavenumber plots obtained by the ITM. a) wavenumber spectrum along the y direction for $k_x = 0$ as a function of the frequency, b) wavenumber spectrum at the frequency step 190 Hz (note that the k_x and the k_y is adapted for better readability), c) wavenumber spectrum at the frequency step 3476 Hz. $f_c = 4000$ Hz, $k_{y,max} = 150$ rad/m, $f_0 = 6000$ Hz.

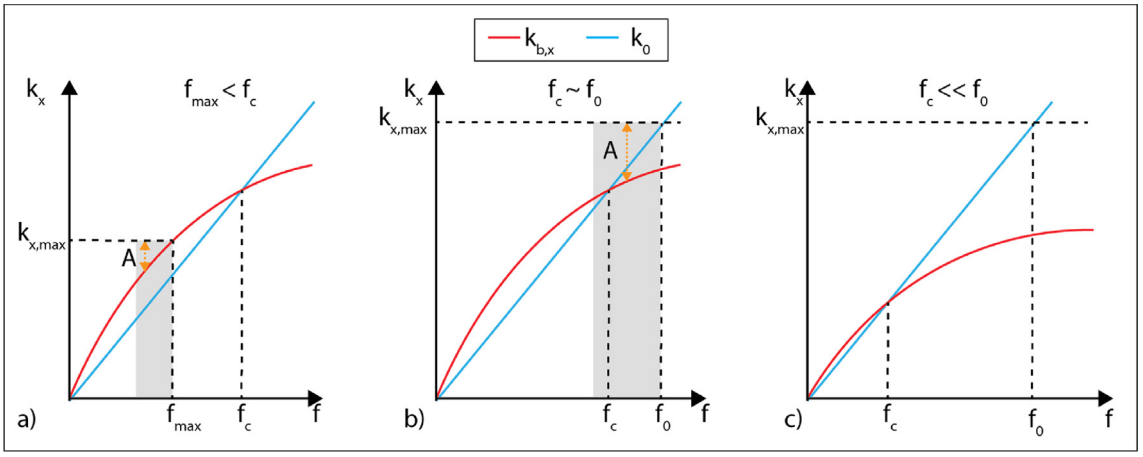

Fig. 2. Key elements to assess the requirements when applying the ITM method. a) show the case where f_{max} is below f_c; b) f_c and f_0 are close to each other on a logarithmic scale; c) f_c is much smaller than f_0. The blue line is the dispersion curve of the sound waves in air. The red line is the dispersion curve of the structural waves in the plate. (For interpretation of the references to color in this figure legend, the reader is referred to the web version of this article.)

tion. The limit describes the situation where the circle reaches the boundaries of the diagram. For higher frequencies, a portion of the circle would be outside of the diagram boundaries causing an information loss and hence possibly corrupting the results. As for the previous case, the limit might be slightly lower depending on the measurement setup and the boundary conditions. Case c): the critical frequency is much lower than the upper frequency limit: $f_c \ll f_0$. The ITM delivers reliable results also above f_0. The reason for this is that for frequencies $f \gg f_c$ the kernel K in Eq. (10) approaches unity:

$$K[\alpha,\beta,\gamma] = \frac{k_0(\gamma)}{\sqrt{k_0(\gamma)^2 - (\alpha\Delta k_x)^2 - (\beta\Delta k_y)^2}} \rightarrow 1 \text{ for } f \gg f_c \qquad (11)$$

This relaxes the requirement set by the Nyquist-Shannon theorem and aliasing can be effectively exploited to extend the measurement range well above the limit f_0. The results in Section 4.2 show an example of this case.

Both in case *a)* and *b)*, the upper limit must be evaluated considering both the bending wave speed and the decay of the side lobes in the wavenumber spectrum. This is highlighted in Fig. 2 with the symbol *A*, indicating the distance between $k_{x,\max}$ and the curve $k_{b,x}$, and the grey area indicating the range where this two lines approach. This distance must be sufficient to let the side lobes decay before reaching $k_{x,\max}$. This distance is dependent on the tested object, its boundary conditions and the measurements settings. An example of the importance of this assessment is presented in Section 4.1, when discussing the grid size required by the all-free-edges (F-F-F-F) boundary conditions.

The ITM offers the advantage of delivering additional material information (e.g. structural wave velocity in the plate) compared to the other methods presented in this paper [13]. Additionally, the measured vibration velocity could also be used to investigate the sound intensity radiated from the element with the supersonic intensity technique [21], which uses the very same data and processing procedure implemented for the ITM.

2.4. Discrete Calculation Method

The Discrete Calculation Method (DCM) is a hybrid approach, proposed by Hashimoto [4] in order to experimentally evaluate the sound power radiated by a planar vibrating structure based on the radiation impedance concept. As the two previous methods, it requires the complex normal vibration velocity $\widehat{v}_{n,i}(\omega,x,y)$ to be measured on a grid of points *i* evenly distributed over the vibrating surface. The sub-elements associated to each measurement position are considered as equivalent radiating pistons; their self Z_{ii} and cross radiation impedances Z_{ij} can be analytically computed as:

$$Z_{ii} = \rho_0 c_0 s_i \left[1 - \frac{J_1(2k_0a_i)}{k_0a_i} + \frac{S_1(2k_0a_i)}{k_0a_i}\right] \tag{12}$$

$$Z_{ij} = \frac{\rho_0 c_0 k_0^2 s_i s_j}{2\pi}\left[2\frac{J_1(k_0a_i)}{k_0a_i}\right]\left[2\frac{J_1(k_0a_j)}{k_0a_j}\right]\left(\frac{sink_0d}{k_0d} + i\frac{cosk_0d}{k_0d}\right) \tag{13}$$

The area of the i^{th} equivalent piston element is s_i, while a_i is its equivalent radius and d is the distance between the i^{th} and j^{th} elements, while J_1 represents the first order Bessel's function, and S_1 is the Struve's function.

Under the assumption of a baffled plate radiating in the free field, the radiated sound power can be determined from the velocity distribution and the self and mutual radiation impedances as:

$$W = \sum_i \left[\mathrm{Re}(Z_{ii})|v_i|^2 + \sum_j \mathrm{Re}(Z_{ij}v_iv_j)\right] \tag{14}$$

where we omitted the subscript n to improve the readability of the equation. In order to obtain the root-mean-square (rms) radiated sound power, as for the RIM and the ITM, the DCM requires as input data the rms complex velocity.

As indicated in the original paper [4], the requirements set by the Nyquist-Shannon theorem must be fulfilled up to at least the critical frequency when the DCM method is used. Above the critical frequency the grid size plays only a minor role on the accuracy of the results.

3. Methodology

As stated in the introduction, we want to accomplish three main tasks: i) numerical benchmark the RIM, ITM and DCM on a simple object considering different boundary conditions, ii) compare the radiated sound power obtained with these three advanced hybrid methods with the radiated sound power determined by impact sound pressure measurements in a standard sound transmission test facilityand iii) to test these three advanced methods on a complex setup and evaluate possible advantages compared to standard laboratory measurements.

In this section, we present the details of the tested setups.

3.1. Benchmark the methods with different boundary conditions

The first task is to benchmark RIM, ITM and DCM on a simple object, i.e. a thin aluminium plate, with different boundary conditions (all edges clamped C-C-C-C, all edges simply supported S-S-S-S, all edges free F-F-F-F, two opposite edges simply supported and two free S-F-S-F). This shall highlight possible limitations or artefacts due to the specific methods.

An aluminium plate (Young's modulus E_{alu} = 7.1 × 1010 N/m^2, density ρ_{alu} = 2700 kg/m^3, Poisson's ratio ν = 0.33, damping factor η = 0.03) with dimensions 0.5 m × 0.6 m × 0.003 m was modelled in the FEM software Abaqus/CAE 2017 (Fig. 3). We used C3D8 general purpose linear brick elements with a maximum mesh size of 0.01 m, which is 10 times smaller than the bending waves wavelength in the aluminium plate at 6000 Hz. The calculations were performed as a steady state linear perturbation with a resolution of 10 Hz from 10 Hz to 5650 Hz so that the results could be evaluated in 1/3 octave bands from 20 Hz to 5000 Hz. The excitation was a harmonic point force distributed over four adjacent nodes at the position $x = l/4$, $y = w/4$. The vibration velocity of the nodes on the bottom face was stored on 120 × 100 grid and evaluated on a variable subset of points, as described in Section 4.1.

The vibration velocity distribution data set produced by the numerical simulation was then fed to Matlab scripts implementing the three methods.

When applying the RIM method, we used a calculation sphere with radius 10 m and 1600 points evenly distributed on its surface.

When applying the ITM method we used a fixed zero-padding factor z_p = 20 for all grid sizes.

3.2. Measurements according to ISO 10140-3

This experimental investigation was performed according to ISO 10140-3 standard on a complex floor structure. The vibration velocity on the bottom side of the plate was measured in addition to the sound pressure in the receiving room.

A timber hollow-box floor element with dimension 2.4 m × 3.7 m × 0.5 m was installed in the vertical sound transmission test facility at the SINTEF acoustic laboratory in Oslo (Fig. 4). The cross-section geometry of the element is shown in Fig. 5 along with the key elements of the measurement setup. The hollow part of the element was partly filled with gravel with a surface mass of approximately 100 kg/m^2. The floor structure was simply supported on the two short sides with an interposed resilient stripe (Sylomer SR55) and free on the two long sides (S-F-S-F).

The floor element was excited at four positions with a standard tapping machine. The sound pressure was measured in the receiving room (V = 200 m^3) with one microphone on a rotating boom at two positions according to ISO 10140-3. The reverberation time was measured accordingly. The radiated sound power was calculating using Eqs. (1) and (2) and averaging energetically the four tapping machine positions according to the standard.

With the same setup, the acceleration in the vertical direction was measured on the bottom surface of the floor element on a 10 × 13 points measurement grid, corresponding to a spacing 0,24 m × 0,28 m (Fig. 5). The corresponding wavenumber limits are: $k_{x,\max}$ = 13 rad/m, $k_{y,\max}$ = 11 rad/m; f_0 = 595 Hz (y-direction).

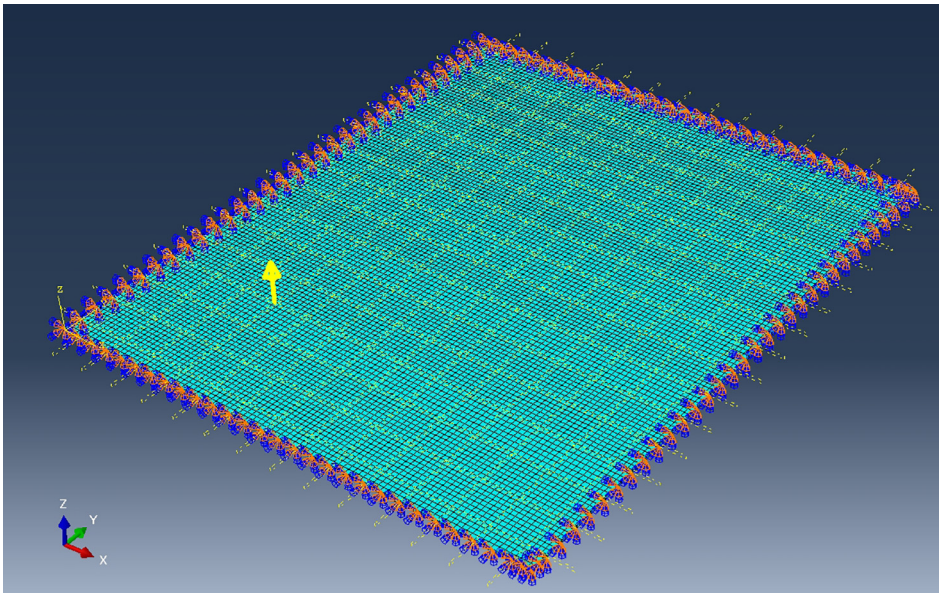

Fig. 3. FE model of the aluminium plate in Abaqus. The mesh (black continuous lines), the evaluation grid (dashed yellow lines), the point load (yellow arrow) and the boundary conditions (C-C-C-C) are shown. (For interpretation of the references to color in this figure legend, the reader is referred to the web version of this article.)

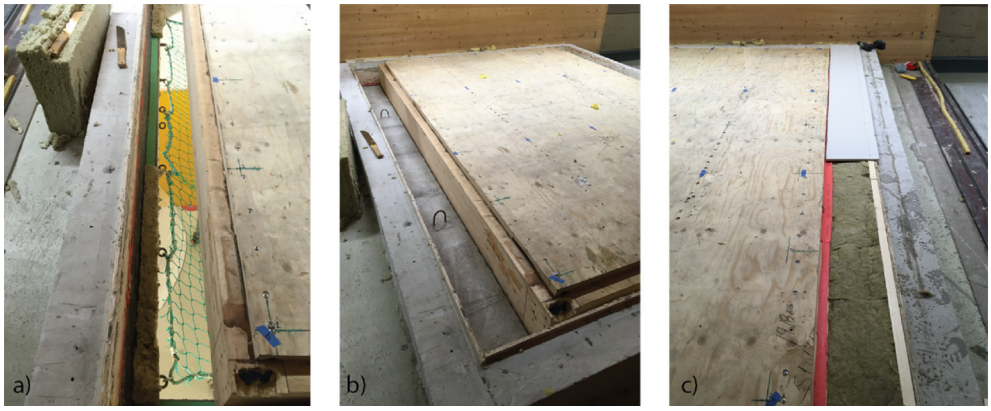

Fig. 4. Three moments of the installation of the test floor into the lab opening: a) positioning of the element (note the S-F-S-F boundary conditions), b) filling of the remaining space with 150 mm concrete and c) sealing of the volume with mineral wool and plasterboard.

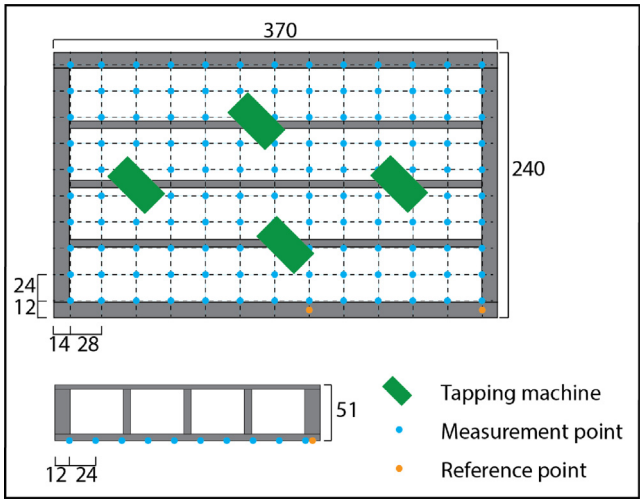

Fig. 5. Schematic of the measurement setup showing the cross section of the measurement objects, the accelerometer positions and the excitation positions. All dimensions in cm.

The critical frequency f_c for this element was determined in (13) as $f_c \cong 250$ Hz. In terms of ITM requirements, this experimental setup is an example of the condition showed in Fig. 2c.

One line (10 points) of the grid was measured at a time, then the tapping machine was moved to the next position and the procedure repeated. After all the excitation positions were covered, the accelerometers were moved to the next line. One additional accelerometer was kept fixed for the whole measurement session as phase reference. The radiated sound power was then calculated for each tapping machine position and the results averaged energetically. The same set of data was analysed with the three methods RIM, ITM and DCM.

When applying the RIM method, we used a calculation hemisphere with radius 10 m, discretised with 1600 points evenly distributed on its surface. When applying the ITM method we used a zero-padding factor $z_p = 60$.

3.3. Application example

Finally, the three methods were tested on a complex setup to evaluate their performance in a "practical" case. The *in-situ* radi-

Fig. 6. Measurement test-rig used for the application example.

ated sound power measured on the complex setup was compared to the radiated sound power determined in laboratory to assess how the laboratory boundary conditions affect the results.

The same floor element, which was tested in the OSLO laboratory, was also installed on the mock-up of a structural system based on moment resisting frames. The mock-up was composed by the floor element mounted on four glulam columns with dimensions 0.4 m × 0.45 m × 5 m by means of threaded rods and metal brackets. The setup is shown in Fig. 6, while the reader may refer to [13] for detailed information on the system.

Table 1
Requirement fulfillment criteria for RIM, ITM and DCM.

RIM criteria:	$\Delta x < \frac{\lambda_{b,x}}{2}, \Delta y < \frac{\lambda_{b,y}}{2}$ @ maximum frequency of interest $f_{max,i}$
ITM criteria:	$f_{max,i} < f_0$ as per case b) in Fig. 2
DCM criteria:	$\Delta x < \frac{\lambda_{b,x}}{2}, \Delta y < \frac{\lambda_{b,y}}{2}$ @ critical frequency f_c

Table 2
Key quantities to evaluate the criteria in Table 1.

Maximum frequency of interest:	$f_{max,i}$ = 5623 Hz, to cover the 5000 Hz 1/3 octave band
Critical frequency:	f_c = 4000 Hz
f_0 (frequency where $k_0 = k_{max}$):	k_0 @ $f_{max,i}$: 104 rad/m
Bending waves @ $f_{max,i}$:	$v_{b,max,i}$ = 408 m/s, $\lambda_{b,max,i}$ = 0.072 m, $k_{b,max,i}$ = 87 rad/m
Bending waves @ f_c:	$v_{b,c}$ = 343 m/s, $\lambda_{b,c}$ = 0.086 m, $k_{b,c}$ = 73 rad/m

We used the same accelerometer configuration and measurement procedure described in Section 3.2. The radiated sound power was determined by the three methods RIM, ITM and DCM. It shall be noted here that the influence of the airborne excitation on the bottom plate due to the noise radiated by the tapping machine exciting the top plate and the corresponding reverberant sound field in the facility was negligible, as discussed in [13].

4. Results

4.1. Assessment of the grid size

In Table 1, we summarize the criteria for the evaluation of the requirements on the grid size for the three methods. In Table 2, we provide the key quantities for the evaluation and in Table 3, we present the criteria assessment for the aluminium plate under investigation evaluated with three different grid sizes: 15 × 10, 30 × 25 and 60 × 50.

We calculated the radiated sound power $L_{w,grid}$ with the three methods RIM, ITM and DCM for the boundary conditions CCCC, SSSS, SFSF, FFFF and the three different grid sizes: 60 × 50, 30 × 25 and 15 × 10 points. Taking as reference the grid 60 × 50, we calculated the level difference

$$\Delta L_W = L_{W,60x50} - L_{w,grid_x}(dB) \quad (15)$$

The results obtained for each case are presented in Fig. 7.

For all the three methods, the results presented in Fig. 7 show a strong dependency of the grid size on the BCs. For the CCCC BCs, no difference is observed between the results obtained with the grid size 60 × 50 and 30 × 25 as expected, since both grid sizes fulfill the criteria over the whole frequency range of interest. The ITM method and the DCM method deliver reliable results even with the larger grid points spacing, which do not fulfill the criteria for the highest frequencies within the range of interest. The Rayleigh method seems to be the most sensitive to the grid size, showing the largest deviations with the smallest grid. With SSSS BCs, small deviations appear for all methods but well within ±1 dB, if the criteria are fulfilled. When the BCs are changed to SFSF and FFFF the deviations increase to more than ±2 dB with the grid size 30 × 25 even though it does fulfill the spatial sampling criteria. The finest considered grid points spacing seems to be required to obtain accurate results.

4.2. Benchmark the methods with varying boundary conditions

Fig. 8 shows the radiation index L_σ of the aluminium plate

$$L_\sigma = 10 \log_{10} \sigma \quad (16)$$

Table 3
Evaluation of the criteria given in Table 1, based on the quantities provided in Table 2.

Dimensions aluminium panel: l = 0.5 m, w = 0.6 m						
Grid points	15 × 10		30 × 25		60 × 50	
Δx, Δy (m)	0.033	0.060	0.017	0.024	0.008	0.012
$\frac{\lambda_{b,max,i}}{2}$	0.036	0.036	0.036	0.036	0.036	0.036
RIM Criteria:	fulfilled	not fulfilled	fulfilled	fulfilled	fulfilled	fulfilled
k_{max} (rad/m)	94	52	188	131	377	262
f_0 (Hz)	5100	2833	10,200	7083	20,400	14,167
ITM Criteria:	not fullfilled	not fullfilled	fulfilled	fulfilled	fulfilled	fulfilled
$\frac{\lambda_{b,c}}{2}$	0.043	0.043	0.043	0.043	0.043	0.043
DCM Criteria:	fulfilled	not fulfilled	fulfilled	fulfilled	fulfilled	fulfilled

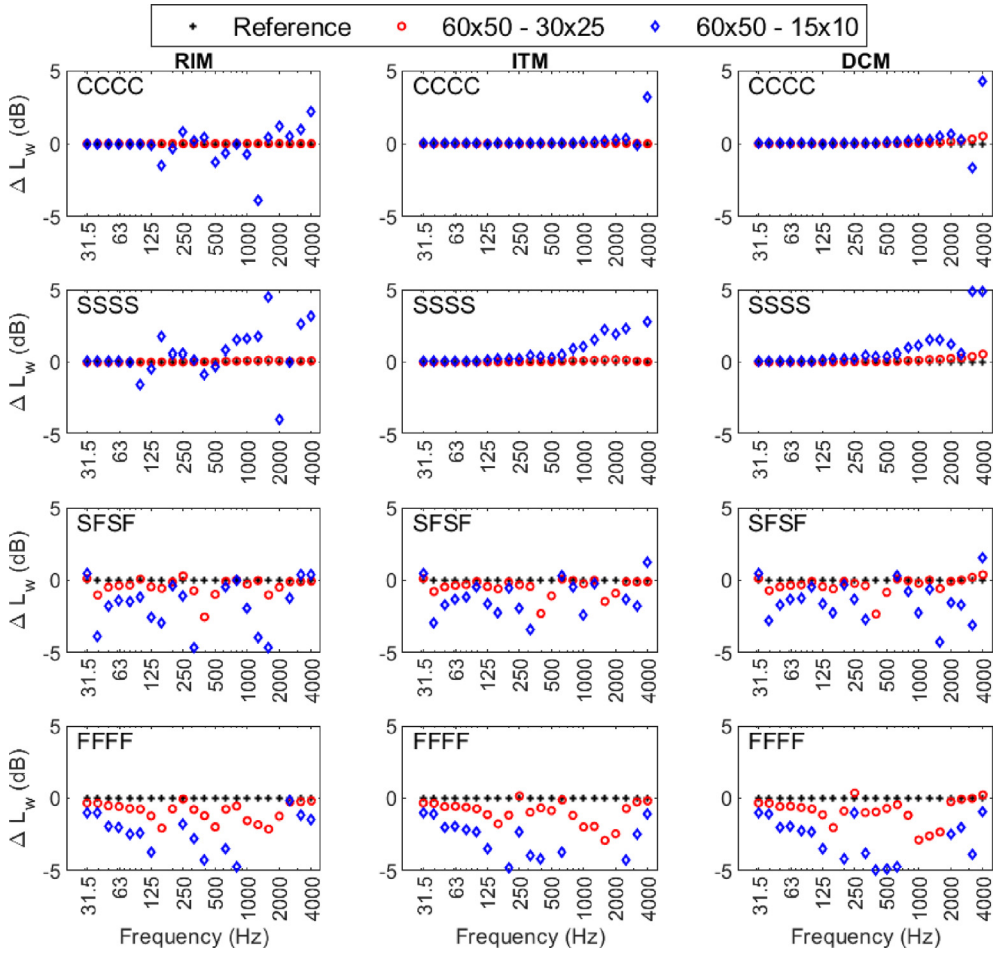

Fig. 7. Difference in the radiated sound power DL_W obtained from different grid sizes for the CCCC, SSSS, SFSF, FFFF BCs, with the methods RIM, ITM and DCM. Grid sizes: 30 × 25, 15 × 10. The differences are calculated by taking the finer grid 60 × 50 as reference.

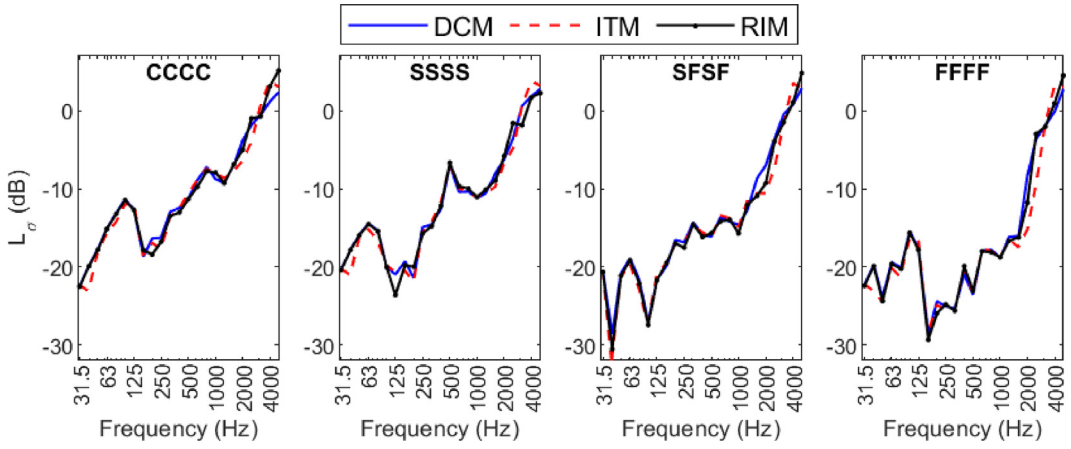

Fig. 8. Comparison of the radiation efficiency calculated with the three methods RIM, ITM and DCM for following boundary conditions: C-C-C-C, S-S-S-S, S-F-S-F, F-F-F-F. Grid size: CCCC and SSSS: 30 × 25; FFFF and SFSF: 60 × 50.

where σ is the radiation efficiency calculated from the vibration velocity distribution obtained from the FE simulation. The three methods were used to calculate the radiation efficiency: ITM, DCM and RIM. The four diagrams present following boundary conditions: all edges clamped (CCCC), all edges simply supported (SSSS), two opposite edges simply supported and two free (SFSF), all edges free boundary conditions (FFFF). Based on the results presented in Section 4.1, we used the grid size 30 × 25 for CCCC and SSSS and 60 × 50 for FFFF and SFSF.

The calculated radiation efficiencies show the expected behaviour (see e.g. [22]) and the results from the three methods show a good agreement. However, it is helpful to plot the differences

between the curves to gain a more detailed view. The two diagrams in Fig. 9 presents the differences in the radiation efficiency for each set of BCs obtained respectively as:

$$\text{a)} \quad \Delta L_\sigma = L_{\sigma,RIM} - L_{\sigma,ITM}(\text{dB}) \tag{17}$$

$$\text{b)} \quad \Delta L_\sigma = L_{\sigma,RIM} - L_{\sigma,DCM}(\text{dB}) \tag{18}$$

where the subscript indicates which method was used to calculate σ. In the diagrams, we also highlight the ±2 dB range using black dashed lines.The comparison between RIM and ITM shows deviations mainly within ±2 dB in the whole frequency range of interest, even though at a few frequency bands the discrepancies are up to 3 dB and in the 3150 Hz 1/3 octave band the deviation is even larger. The same observation can be made for all BCs, even though, the deviations seem to increase with FFFF BCs. The comparison between RIM and DCM shows a good agreement and highlights a slightly increasing deviation between the results as the frequency increases. The discrepancies between the methods might be related to the near field generated by the excitation used: excitation by a harmonic concentrated force as in this case, generates a strong nearfield comparable to that generated by a shaker in an experimental setup [23]. A nearfield is a local feature of the vibrational field. Local features are described by the high frequency components of the spectrum and due to the finite size of the grid these features can be reproduced only to a limited extent [16]. The sensitivity of the methods to these effects is different due to their different mathematical implementation and it might be worth of further investigation.

As we have seen in the previous section, the grid size must be adapted to the BCs for all the three investigated methods. Possible deviations from the reference radiated sound power might happen at different frequencies for the different methods and the different BCs. This prevent us from making an absolute reliability ranking of these methods.

The ITM results could be further investigated by studying the wavenumber spectra. Each color plot in Fig. 10 shows the vibration velocity wavenumber spectrum multiplied with the kernel K, given in Eq. (11), in the format k_x (longitudinal direction) versus frequency at $k_y = 0$. At each frequency step the amplitude was normalized to the maximum in the same frequency step. Data are shown in dB with a 10 dB range. The black dashed line shows the wavenumber for bending waves calculated according to the thin plate theory. The solid white line indicates the wavenumber of the sound waves in air. The area within the two white lines contributes to sound radiation. The plots are presented for two boundary conditions and two grid sizes: a) CCCC, 30 × 25; b) FFFF 30 × 25; c) CCCC, 60 × 50; d) FFFF, 60 × 50.

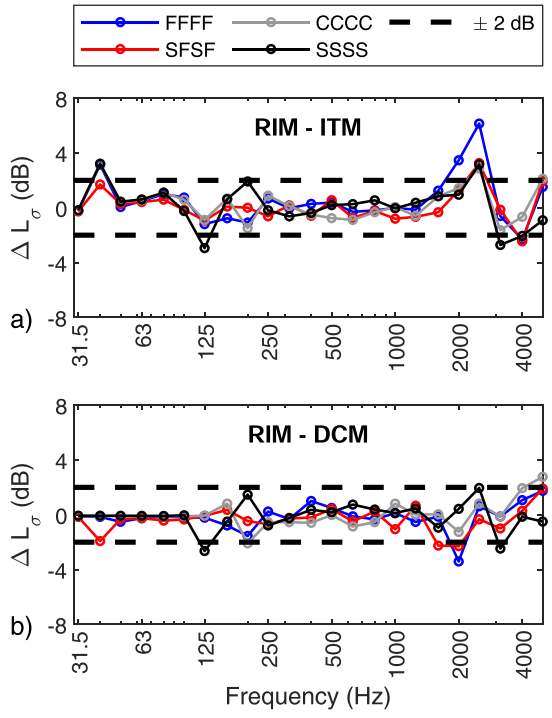

Fig. 9. Differences between radiation efficiency σ calculated by a) RIM and ITM and b) by RIM and DCM, for different boundary conditions. Grid size: see Fig. 8.

The diagrams a) and c) in Fig. 10 clearly show the dispersion curves of the bending waves and higher order lamb waves. The curves in a) and c) are nearly identical confirming that a 30 × 25 grid is in this case appropriate to avoid aliasing effects with CCCC BCs. The diagrams b) and d) in Fig. 10 differs strongly in the area between the two white solid lines (e.g. the features highlighted with the red arrows in b)). This indicates that a 30 × 25 grid is in this case not sufficient to avoid aliasing effects with FFFF BCs. A larger 60 × 50 grid is then mandatory to obtain reliable results. An even larger grid or higher z_p might slightly improve the accuracy of the results but at a higher computational cost.

4.3. Measurements according to ISO 10140-3

In Fig. 11, we compare the radiated sound power level, obtained from sound pressure measurements performed in a sound transmission test facility according to the standard ISO10140-3 (ISO), with the results obtained from vibration velocity measurements, performed on the very same setup and analysed with the RIM, ITM and DCM approaches. In the upper diagram the sound power level L_w obtained by each method is presented. As explained in Section 2.1, the impact noise level obtained by the standard method was converted to a radiated sound power level assuming a perfectly diffuse sound field, by means of Eq. (2). To ease the comparison, we show in the lower graph the respective difference between each curve and the ISO curve.

We observe, in general, a good agreement between the methods within the frequency range in which the requirements of the methods are fulfilled. We observe that below 125 Hz the vibration velocity-based measurement methods are in close agreement with each other but clearly deviate from the results based on sound pressure measurements. The limitation here are not the measurement methods, but the diffuse field assumption, which is required to convert the sound pressure levels into the radiated sound power levels. This assumption is not valid at low frequencies in our measurement setup. The requirements set by the Nyquist-Shannon theorem are met up to approximately 500 Hz on this setup [13]. We clearly observe that the Rayleigh methods fails above this frequency, due to the introduced aliasing effects. ITM and DCM still deliver reliable data as expected. Above 4000 Hz, both the DCM and the ITM deviate from the standard results but they agree with each other. We suspect that this has to do with the experimental setup and the mounting of the accelerometers.

It is interesting at this point to compare the results presented in Fig. 11 with the results presented in Figs. 8 and 9. The results from the experimental setup show smaller deviations between the methods as compared to the results from the numerical simulation. In fact, the deviations between ITM and DCM are well within ±2 dB in the experimental situation, while the ±2 deviation was exceeded in several frequency bands in the numerical simulation results. One possible reason for the better agreement might be that in the experimental case no near field effects are expected, mainly because of the larger distance between excitation point and measurement points [23]. In addition, the larger spatial extension of the experimental excitation (the length of the tapping machine is

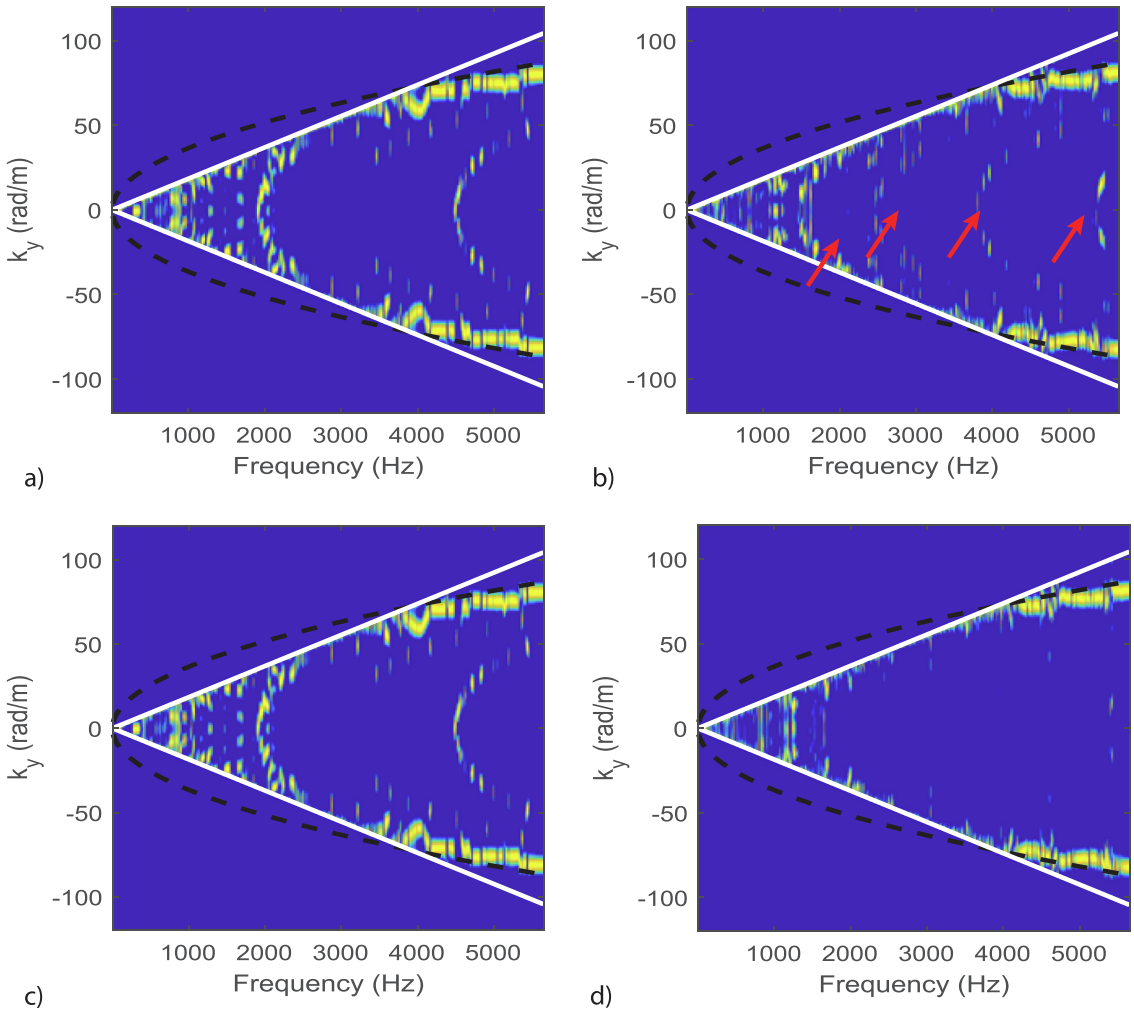

Fig. 10. Wavenumber spectrum of the product K · v (Eq. 10) plotted for $k_y = 0$, normalized to the maximum amplitude at each frequency step. BCs and grid sizes: a) CCCC, 30 × 25; b) FFFF 30 × 25; c) CCCC, 60 × 50; d) FFFF, 60 × 50. In b) the red arrows mark the aliasing effects. (For interpretation of the references to color in this figure legend, the reader is referred to the web version of this article.)

0.5 m) compared to the point excitation of the simulation was probably able to excite a larger number of modes within the considered frequency range, smoothening the peaks and the dips caused by the resonances. The averaging between tapping machine excitation position goes in the same direction. Both aspects possibly reduce the discrepancies between the methods.

These results demonstrate that all three methods RIM, ITM and DCM are valuable alternatives to the standard method to determine the radiated sound power of a planar object due to impact excitation. Neither the boundary conditions, nor the sequential excitation by the tapping machine at several positions, nor the shifting of the accelerometers over the measurement grid appear to be limiting factors to the application of the methods.

4.4. Application example

As an application example, we present in this section the results obtained by ITM and DCM for the same floor element installed in two different situations: in a standard laboratory setup (Oslo) and on a moment resisting frame (CVGS). We exclude RIM from the comparison in this case due to its limited frequency range of validity.

Fig. 12 shows the radiated sound power obtained for the same floor in the two different situations by ITM (a) and DCM (b).

Both methods deliver results in close agreement and can identify the specific radiation properties of the tested setups. The radiated sound power obtained in the Oslo laboratory and at CVGS are almost identical above 500 Hz. Below 500 Hz, the modal behaviour of the floor elements on the two setups differs because of the different boundary conditions and this affects the radiated sound power. Between 100 Hz and 500 Hz the radiated sound power level is up to 3 dB higher with the CVGS BCs. Between 50 Hz and 100 Hz the radiated sound power level is up to 4 dB lower with the CVGS BCs. In the 31.5 Hz 1/3-octave band and below 25 Hz forced vibration introduced by the undampened columns of the CVGS setup determine the high radiation peaks. Both the ITM method and the DCM method can catch these features.

5. Conclusions

We presented three measurement methods suitable to determine the radiated sound power from planar objects and benchmarked them in the special case of mechanical excitation, either by a point force or by a tapping machine. We discussed in detail the limit of validity of the methods and presented relevant examples.

The comparison of the methods was firstly performed based on numerical data computed for an aluminium plate with vary-

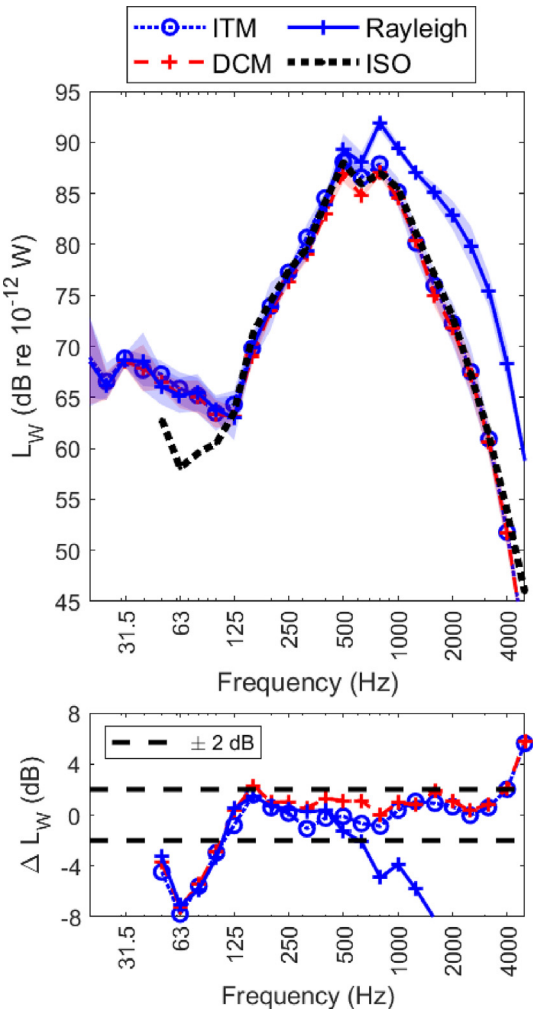

Fig. 11. Comparison of the three methods RIM (Rayleigh), ITM, DCM with the radiated sound level obtained from the impact sound level measured according to the standard ISO10140-3 on a S-F-S-F lab setup.

ing boundary conditions. The benchmarking of the three methods RIM, ITM and DCM on such a simple object showed a general good agreement between the methods over the whole frequency range of interest, with discrepancies mainly within ±2 dB, even though higher deviations were found in certain frequency bands. The required grid size resulted to be dependent on the BCs for all methods. F-F-F-F boundary conditions requires a finer grid to accurately evaluate the radiated sound power compared to boundary conditions restraining the edges to a higher degree.

The three considered methods were then applied to an experimental data set, measured in laboratory conditions on a complex floor structure under impact excitation by a tapping machine. We compared the sound power levels computed by means of these three hybrid methods with the sound power obtained from sound pressure measurements in a standard sound transmission test facility according to the ISO 10140-3 standard. A good agreement between the methods was found from 20 Hz to 4000 Hz, as long as the validity requirements of the methods were fulfilled. No limitations were observed due to the sequential repositioning of the tapping machine or the position shifting of the accelerometers.

Finally, the ITM and DCM methods were applied to a complex experimental setup, showing that they provide accurate results and they are consistent with each other also for in situ conditions. We showed that these methods can be used to obtain accurate

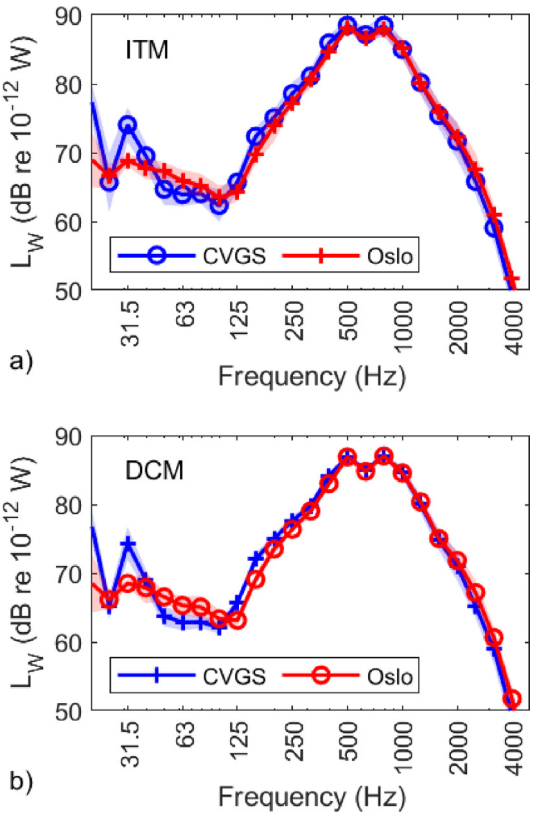

Fig. 12. Sound power level measured in the acoustic lab (Oslo) and "in situ" (CVGS) with ITM a) and DCM b).

information on the specific experimental setup. This is an advantage compared to the standard laboratory setup, since they require reduced practical constraints.

CRediT authorship contribution statement

Simone Conta: Conceptualization, Methodology, Software, Investigation, Writing - original draft. **Andrea Santoni:** Writing - review & editing, Software. **Anders Homb:** Writing - review & editing, Supervision.

Declaration of Competing Interest

The authors declare that they have no known competing financial interests or personal relationships that could have appeared to influence the work reported in this paper.

Acknowledgments

This study has been carried out within the Woodsol project, a project funded by The Research Council of Norway and leaded by Kjell Arne Malo at NTNU. The project include research at NTNU and SINTEF Building & Infrastructure and the PhD grant for the first author of this paper, which is gratefully acknowledged. Petra Rüther at SINTEF was work package leader for "WP6 Prototype", which made the prototype possible. Sveinung Nesheim and Aivars Vilguts, both PhD students at NTNU and member of the Woodsol project, were involved in the design and construction of the WOODSOL prototype. Leif Joar Lassesen and students from Charlottenlund Videregående skole in Trondheim (NO) greatly supported us during the construction of the prototype. The laboratory team at SINTEF Community in OSLO supported us during the measurement in Oslo.

References

[1] ISO10140-3:2010. Acoustics — Laboratory measurement of sound insulation of building elements — Part 3: Measurement of impact sound insulation.
[2] Ljunggren F, Simmons C, Öqvist R. Correlation between sound insulation and occupants' perception – Proposal of alternative single number rating of impact sound, part II. Appl Acoust 2017;123:143–51.
[3] Rayleigh JWSB. The theory of sound. New York: Dover Publications; 1945.
[4] Hashimoto N. Measurement of sound radiation efficiency by the discrete calculation method. Appl Acoust 2001;62(4):429–46.
[5] Heckl M. Radiation from plane sound sources. Acta Acustica United Acustica 1977;37(3):155–66.
[6] Revel GM, Rossi GL. Sound power estimation by laser Doppler vibration measurement techniques. Shock Vib 1998;5(5–6).
[7] Roozen NB, Labelle L, Rychtáriková M, Glorieux C. Determining radiated sound power of building structures by means of laser Doppler vibrometry. J Sound Vib 2015;346:81–99.
[8] Santoni A, Fausti P, Schoenwald S, Tröbs H-M, editors. Sound radiation efficiency measurements on cross-laminated timber plates. INTER-NOISE and NOISE-CON Congress and Conference Proceedings; 2016: Institute of Noise Control Engineering.
[9] Santoni A, Schoenwald S, Van Damme B, Fausti P. Determination of the elastic and stiffness characteristics of cross-laminated timber plates from flexural wave velocity measurements. J Sound Vib 2017;400:387–401.
[10] Schoenwald S, Vallely S, Tröbs H-M. Advanced methods to determine sound power radiated from planar structures. J Acoust Soc Am 2017;141(5):3713.
[11] Kohrmann M. Numerical methods for the vibro-acoustic assessment of timber floor constructions [Dissertation]: Technische. Universität München; 2017.
[12] Marchetto C, Maxit L, Robin O, Berry A. Vibroacoustic response of panels under diffuse acoustic field excitation from sensitivity functions and reciprocity principles. J Acoust Soc Am 2017;141(6):4508–21.
[13] Conta S, Homb A. Sound radiation of hollow box timber floors under impact excitation: an experimental parameter study. Appl Acoust 2020;161:107190.
[14] Vigran TE. Building acoustics. CRC Press; 2014.
[15] Cremer L, Heckl M, Petersson BA. Structure-borne sound: structural vibrations and sound radiation at audio frequencies. Springer; 2005.
[16] Bies DA, Hansen C, Howard C. Engineering noise control. CRC Press; 2017.
[17] Williams EG, Maynard JD. Numerical evaluation of the Rayleigh integral for planar radiators using the FFT. J Acoust Soc Am 1982;72(6):2020–30.
[18] Fuller CC, Elliott S, Nelson PA. Active control of vibration. Academic Press; 1996.
[19] Maynard JD, Williams EG, Lee Y. Nearfield acoustic holography: I. Theory of generalized holography and the development of NAH. J Acoust Soc Am 1985;78(4):1395–413.
[20] Conta S, Homb A, editors. Challenges and limitations using the Integral Transform Method to obtain the impact noise level of timber floors. Euronoise 2018; 2018; Creta.
[21] Williams EG. Chapter 2 - Plane Waves. Fourier Acoustics. London: Academic Press; 1999. p. 15–87.
[22] Squicciarini G, Thompson DJ, Corradi R. The effect of different combinations of boundary conditions on the average radiation efficiency of rectangular plates. J Sound Vib 2014;333(17):3931–48.
[23] Davy JL, Mahn JP, Guigou-Carter C, Villot M. The prediction of flanking sound transmission below the critical frequency. J Acoust Soc Am 2012;132(4):2359–70.